Phase Transitions in Orthopyroxene (En_{90}) to 49 GPa from Single-Crystal X-Ray Diffraction

Gregory J. Finkelstein[1*], Przemyslaw K. Dera[2, 3], and Thomas S. Duffy[1]

[1]Department of Geosciences, Princeton University, Princeton, NJ 08544, USA

[2]Hawaii Institute of Geophysics & Planetology, School of Ocean and Earth Science and Technology, University of Hawaii, 1680 East West Road (POST Bldg 819E), Honolulu, Hawaii 96822, USA

[3]GSECARS, University of Chicago, Building 434A, 9700 South Cass Avenue, Argonne, Illinois 60439, USA

Key Words: orthopyroxene; phase transition; crystallography; high pressure; single-crystal X-ray diffraction

Abstract

Synchrotron-based high-pressure single-crystal X-ray diffraction experiments were conducted on ~$Mg_{0.9}Fe_{0.1}SiO_3$ (En_{90}) orthopyroxene crystals at room temperature to a maximum pressure of 48.5 GPa. The sample was compressed in a diamond anvil cell with a neon pressure-transmitting medium and a gold pressure calibrant. In addition to the previously described orthopyroxene to β-opx transition (designated HPCEN2 in previous studies), we observe two further phase transitions at 29.9 GPa and 40.3 GPa. However, we do not observe the γ-opx phase recently described in an Fe-rich orthopyroxene composition. The structures of both of the new phases were solved in space group $Pca2_1$. While their Mg-O layers remain pyroxene-like, their Si-O layers transform in a stepwise fashion to akimotoite-like sheets, with sites in 4-, 4+1-, or 6-fold coordination, depending on the specific structure and layer. Due to the increased Si-O coordination number, we designate the new structures α- and β-post-orthopyroxene (α-popx and β-popx). α-popx has one Si-O layer that is entirely tetrahedral, and one layer that contains both tetrahedra and 4+1-coordinated Si in distorted square pyramids. β-popx retains the mixed 4- and 4+1-coordinated Si layer found in α-popx, while the other Si layer adopts fully octahedral coordination. The α- and β-popx structures show a progressive transformation towards the arrangement of Si layers found in akimotoite, a potentially important phase in the earth's transition zone. Metastable transformations in pyroxenes are of interest for understanding possible metastability in geological environments such as subducting slabs and meteorite impacts.

Introduction

Pyroxenes with compositions of $(Mg,Fe)SiO_3$ are important minerals in the Earth's crust and mantle, as well as in meteorites. In the crust, they are found in mafic igneous rocks and in metamorphic rocks, including granulites from the lower crust. $(Mg,Fe)SiO_3$ polymorphs are major components of the mantle at all depths. Petrological models for the upper mantle contain ~20% opx on average (Ringwood, 1975), while opx-dominated pyroxenites may contribute to heterogeneity on the local or regional scale. Phase transformations in pyroxenes have been identified as a possible cause or contributor to seismic discontinuities in the mantle such as the "X" discontinuity at ~300 km depth (Woodland, 1998). Pyroxenes are also a major constituent of the harzburgites that make up a large portion of subducting lithosphere (Ringwood, 1982). Under the cold temperatures of subducting slabs, pyroxenes may remain metastable to transition zone depths (Hogrefe et al., 1994; Nishi et al., 2008; van Mierlo et al., 2013). Such metastable phases may add buoyancy to the slabs, resulting in slowed subduction and/or transient stagnation. Direct transformation of metastable pyroxene to the dense high-pressure phase akimotoite in the lowermost upper mantle may occur, possibly promoting rapid penetration of stagnant slabs into the lower mantle (Hogrefe et al., 1994).

Pyroxenes are characterized by chains of corner-sharing SiO_4 tetrahedra that extend in the crystallographic *c*-direction. These are interleaved with ribbons of two different types of MO_6 octahedra, the more regular M1 and more distorted M2 sites. (When large cations such as Ca^{2+} reside in the M2 site, they are 8-coordinated.) The basal triangles of the octahedra can point in either the $+c$ direction or the $-c$

direction, called "+" and "–" tilt, respectively. The tetrahedral chains can be either unkinked (extended) or kinked in one of two different ways (designated O- and S-rotation) (Papike et al., 1973; Thompson, 1970). Furthermore, the manner in which the tetrahedral chains are laterally attached to adjacent M1 octahedra puts constraints on the geometry of the M2 site (Sueno et al., 1976). The stacking between layers with different octahedral tilting directions determines whether a given pyroxene is an orthopyroxene (opx) or a clinopyroxene (cpx). Here, we focus on the room-temperature high-pressure polymorphism of Mg-rich orthopyroxene.

The opx structure, shown in figure 1, has *Pbca* symmetry. Two symmetrically distinct tetrahedral Si chains, A and B, are interleaved between octahedral Mg layers. Both the A and the B chain are O-rotated, with the B chain being strongly O-rotated and the A chain in nearly an extended configuration. In opx, the Mg octahedra switch to the opposite tilting direction every two octahedral layers, leading to a unit cell that is approximately doubled in the *a* direction compared to cpx.

At high pressures and temperatures, opx transforms into $C2/c$ cpx (Angel et al., 1992; Kanzaki, 1991; Pacalo and Gasparik, 1990) at ~9 GPa. Depending on temperature, it undergoes further transformations into other phases such as majorite, wadsleyite + stishovite, and akimotoite before ultimately transforming to the perovskite structure (Fei and Bertka, 1999). Cold compression of crystalline materials can result in the kinetic inhibition of phase transitions in favor of metastable structures with energetically lower transformation pathways. The compression behavior of opx at 300 K is now well characterized below 10 GPa

93 (Angel and Jackson, 2002; Periotto et al., 2012), but is only starting to be elucidated
94 above this pressure.
95 Previous ultrasonic elasticity measurements (Kung et al., 2004) and Raman
96 spectroscopy (Lin, 2003; Serghiou, 2003) at room temperature reported that the
97 Mg-endmember of opx, enstatite (En), persists to ~12 GPa, with a possible phase
98 transition occurring above this pressure. Subsequent Mössbauer spectroscopy by
99 Zhang et al. (2011) on En_{87} (87 mol % of enstatite) described changes in the
100 hyperfine parameters at 10 GPa that also suggested the occurrence of a phase
101 transition. The structure of the new phase was solved by Zhang et al. (2012) using
102 single-crystal X-ray diffraction. This structure, which we call β-opx (designated
103 HPCEN2 in earlier studies), is related to a structure predicted by molecular
104 dynamics simulations and DFT calculations (Jahn, 2008), and has $P2_1/c$ monoclinic
105 symmetry. Despite its lower symmetry, it retains an opx-like ++--++-- octahedral tilt
106 pattern, distinguishing it from a true cpx (++++). In contrast with opx, however, it
107 has four symmetrically distinct Si chains. The lowering of symmetry from *Pbca* to
108 $P2_1/c$ is a result of one of the initial A-chains becoming S-rotated, while the other
109 remains O-rotated. These mixed O- and S-rotated A-chain layers are similar to those
110 seen in a high-pressure $P2_1cn$ polymorph of protopyroxene (Yang et al., 1999).
111 Subsequent studies have examined other aspects of the opx to β-opx phase
112 transition. Using Raman spectroscopy, it was shown that in nearly Fe-free opx the
113 transition to β-opx occurs at ~13 GPa, but that the presence of Fe lowers the
114 transition pressure (Zhang et al., 2013b). Incorporation of Al and Ca into opx has the
115 opposite effect and increases the transition pressure for an En_{90} composition.

Additional Raman work has investigated the pressure-temperature slope of the phase boundary and the stability of β-opx at high temperature (Zhang et al., 2014). The elastic properties and lattice dynamics of β-opx were studied using synchrotron-based nuclear resonant inelastic scattering and powder X-ray diffraction (Zhang et al., 2013a).

Another recent study on an Fe-rich En_{16} opx composition reported transitions from opx to β-opx at 11.1 GPa, and then from β-opx to a second high-pressure phase, γ-opx, at 13.0 GPa (Dera et al., 2013a). The initial opx *Pbca* symmetry is regained in the γ-phase as a result of the second A-chain in the structure becoming *S*-rotated (this is the main structural difference between β- and γ-opx). These high-pressure 300-K structures were shown to be thermodynamically metastable in comparison with *C*2/*c* cpx (Li et al., 2013). In this study, we use single-crystal X-ray diffraction to extend examination of the 300-K compression behavior of Mg-rich opx to higher pressures, and to search for further structural changes.

Methods

A natural crystal with composition $Mg_{0.900}Fe_{0.088}Ca_{0.003}Mn_{0.003}Al_{0.004}Si_{0.999}O_3$ (En_{90}) opx was used as a starting material. The sample was characterized at ambient conditions by X-ray diffraction, Raman spectroscopy, and electron microprobe analysis (Table 1). The material used here is from the same parent crystal as the sample used in the study by Dorfman et al. (2013). Small fragments (≤10 μm thick) from a larger single crystal were extracted for our experiments. The unit cell parameters at ambient pressure are a = 18.249(2) Å, b = 8.8263(9) Å, and c = 5.1858(3) Å, in good agreement with literature values (Tarantino et al., 2002).

Synchrotron X-ray diffraction experiments were performed at the Advanced Photon Source (APS), Argonne National Laboratory. Ambient–pressure X-ray experiments were carried out at the 16-ID-B beamline (HPCAT), while high-pressure experiments were performed at 13-ID-D (GSECARS). Pressure was generated using a symmetric-type diamond anvil cell with 300-μm culets. The sample chamber (figure 2) was formed by drilling a ~170-μm hole through a rhenium gasket that was pre-indented to ~35 μm in thickness. Five orthopyroxene crystals (~10-20 μm in diameter) were loaded into the sample chamber. An annealed ruby sphere and a gold foil (~10-μm thick) were also included for pressure calibration. The ruby sphere was chosen to be thicker than the sample crystals, so that if the ruby did not bridge between the diamonds at high pressure, neither would the sample crystals. The pressures listed in Table 2 are based on the gold pressure scale of Fei et al. (2007). We used only the (111) line of gold, as this peak is relatively insensitive to differential stress (Takemura and Dewaele, 2008). For consistency, data from only one of the opx crystals is reported in this paper (Fig. 2), but other crystals showed similar behavior. To achieve quasi-hydrostatic conditions, the cell was loaded with a neon pressure-transmitting medium using the GSECARS/COMPRES gas-loading system. Rare-gas solids such as neon provide optimum quasi-hydrostatic conditions at high pressures (Angel et al., 2007). To enhance reciprocal space coverage at high pressures, a cubic boron nitride (cBN) backing plate (seat) was used with the upstream diamond, while a tungsten carbide (WC) seat with a 60^{o} opening angle was used with the downstream diamond.

Monochromatic diffraction experiments were performed at HPCAT using X-rays with a wavelength of 0.3515 Å and at GSECARS with a wavelength of 0.2950 Å. The beam was focused to less than 10 x 10 μm by Kirkpatrick-Baez mirrors at each beamline. Diffraction patterns were collected using a Mar CCD detector that was calibrated with a LaB_6 standard using the program FIT2D (Hammersley et al., 1996). At each pressure, a wide and stepped scan about the vertical axis of the diffractometer (ω scan) were collected for each crystal. Wide scans consisted of four 12° rotations of the diamond cell in ω while the detector was exposed (covering 48° in total, a range dictated by the geometrical opening of the cell). These were used to extract *d*-spacings, azimuthal angles around the beam center, and peak intensities. The step size of the wide ω rotation was chosen to be small enough so as to minimize peak overlap, but large enough to minimize timing errors between the rotation and the X-ray shutter. Step scans consisted of individual exposures taken at 1° intervals to constrain the ω angle of maximum intensity for each peak. This provides the third dimension necessary for reconstructing the crystal's reciprocal lattice and indexing the diffraction pattern. Both wide and step scans were collected at the central detector position, as well as at positions shifted horizontally ±70 mm in order to increase spatial coverage. A total of 15 pressure steps were carried out to a maximum pressure of 48.5 GPa. The stress state in the sample chamber remained quasi-hydrostatic to the maximum pressure achieved, as evidenced by only a slight broadening of the ruby fluorescence peaks at the highest pressures.

Peak fitting was performed using the program GSE_ADA (Dera et al., 2013b). Polarization, Lorentz, and a correction for absorption by the diamond cell

components were applied to the fit peaks. The DAC absorption correction was determined empirically by measuring the downstream beam intensity as the cell was rotated in the X-ray beam. Positions and intensities for ~400-600 unique peaks were extracted from the raw diffraction patterns at each pressure point. The unit cell, orientation matrix, and where necessary, twin laws, were found using the program CELL_NOW (Bruker AXS Inc.). Transformations to conventional unit cells were determined using XPREP (Bruker, 2007), and lattice parameters were refined using a least-squares fitting procedure in the program RSV (Dera et al., 2013b).

Partial crystal structures for new phases were solved using Endeavor (Brandenburg and Putz, 2009; Putz et al., 1999). SHELX-2013 (Sheldrick, 2008) was used first to determine the locations of residual electron density holes in order to fully solve the new structures, and then to carry out complete crystal-structure refinements at selected pressures. X-ray anomalous dispersion corrections were carried out using the program XDISP (Kissel and Pratt, 1990). The Mg/Fe ratio was refined only for the pyroxene M2 site(s). The other cation sites already had site occupancies less than 1 (but greater than 0.9) due to a combination of small quantities of defects and chemical substitutions (e.g. Al, Mn, etc.). Displacement parameters were refined isotropically. Representative structural data are presented in Tables 1-4 and Supplementary Material.

The PATHFIND executable of the program SPEEDEN (Downs et al., 1996) was used to calculate procrystal electron density distributions for high-pressure phases and to determine cation-oxygen bond paths from them using bond-critical point analysis (Bader, 1990; Bader, 1998). Procrystal electron density distributions

use superimposed spherical electron density distributions at atomic positions to model a crystal's electron density distribution, and have been shown to agree well with *ab initio* studies (Downs et al., 2002). A bond path is defined as a line that connects two atoms such that every point along its length is a local maximum in electron density in the perpendicular plane. Thus, a bond between two atoms exists only if a saddle point (critical point) in electron density between them can be found. The bonds identified by SPEEDEN were used as the basis for assigning coordination polyhedra to cations. Geometrical parameters of these polyhedra were calculated using XtalDraw (Downs et al., 2003).

Results and Discussion

Three phase transitions were observed in En_{90} opx up to 48.5 GPa (figure 3). We observe the previously reported transition to β-opx between 10.1 and 14.6 GPa, followed by two additional transformations, one between 26.9 and 29.9 GPa, and another between 36.8 and 40.3 GPa, to previously unreported structures. The volume reductions observed across each transition are 3.5%, 2.5%, and 3.9%, respectively. The two new structures both have orthorhombic space group $Pca2_1$ symmetry, as evidenced by systematic absences, structure solution, and structure refinement. We designate them α-post-orthopyroxene and β-post-orthopyroxene (α- and β-popx), respectively, for reasons discussed below. While the refinement parameters reported below are in $Pca2_1$, the lattice parameters, structure images, and discussion of structural features use a $P2_1ca$ configuration instead, so that the directions of unit cell basis vectors are the same for all structures from opx to β-popx. The transformation matrix between $Pca2_1$ and $P2_1ca$ is:

$$\begin{bmatrix} 0 & 0 & 1 \\ 0 & 1 & 0 \\ -1 & 0 & 0 \end{bmatrix}$$

The space group $Pca2_1$ has been previously suggested as a possibility for pyroxenes that lose symmetric equivalence between the Si chains in each layer (i.e. the A and B chains split into two symmetrically distinct chains, designated Aa/Ab and Ba/Bb) (Thompson, 1970). Initially, Smyth (1974) reported evidence for a structure with this space group in a lunar opx, but Domeneghetti et al. (1996) later showed that this sample was actually a mixture of *Pbca* opx and exsolved $C2/c$ cpx. Our work therefore is the first observation of a pyroxene-like $Pca2_1$ structure.

Figure 4 shows the volume compression of En_{90} opx compared with previous single-crystal studies on En_{100} to 8.5 GPa (Angel and Hugh-Jones, 1994; Angel and Jackson, 2002) and En_{16} (Dera et al., 2013a) to 32.3 GPa (also see Table 2). All three datasets show similar compression behavior for the initial opx structure, but En_{16} undergoes a sequence of phase transitions from α- to β- to γ-phase over a narrow pressure interval from 10.1-13.0 GPa, and thus exhibits a higher total degree of compression than En_{90} up to 29 GPa, the pressure where En_{90} transforms from β-opx to α-popx.

Figure 5 compares the axial compression behavior of the En_{90} and En_{16} compositions (also see Table 2). For the initial opx structure the *b*-direction is the most compressible and the *a*-direction the least. In contrast, looking at absolute compression across phase boundaries over the entire measured pressure range, in both the Fe-rich and Fe-poor compositions the *c*-direction undergoes the most overall compression and the *a*-direction the least. The compression trends are

similar for both compositions. In En_{90}, the *a*-direction increases slightly across each transition boundary, with a maximum increase of ~0.7% between β-opx and α-popx. For the transitions to β-opx and α-popx, the volume reduction is due to reduction in the *c*-axis, as the *a*- and *b*-directions either slightly increase in length or do not change significantly. The combined discontinuity in the *c*-direction from these two transitions is ~5.7%. The *c*-direction discontinuously changes an additional ~1.5% across the *a*- to β-popx transition, but most of the volume change across that transition is taken up by the *b*-direction, with a length reduction of ~2.5%.

One feature of the opx to β-opx phase transition that was previously described by Dera et al. (2013a) is twinning of the β-phase (Figure 3b). We observe similar phase transition-induced non-merohedral twinning in our low-Fe composition. The twinning is inherent to the phase transition as a result of the reduction from orthorhombic *Pbca* symmetry to monoclinic $P2_1/c$ symmetry.

We did not observe the γ-opx phase described by Dera et al. (2013a) for the En_{16} opx composition at 14.6 GPa. Instead, β-opx persists in En_{90} opx to 26.9 GPa, ruling out the possible existence of metastable γ-opx for the range of Fe contents expected in the mantle. However, at 29.9 GPa, a change in the diffraction pattern occurred and the α-popx phase was observed (Figure 6, Table 3). Since the pressure step between β-opx and α-popx was fairly large, ~3 GPa, it is possible we overstepped a narrow region in which γ-opx forms. We suspect this might be the case because *Pbca*, the space group of γ-opx, is a common direct supergroup of both $P2_1/c$, the space group of β-opx, and $Pca2_1$, the space group of α-popx, whereas no

direct supergroup-subgroup relation exists between the space groups of β-opx and α-popx. In addition, the non-merohedral twinning present in the β-opx crystal disappears on transition to α-popx, implying an intermediary with higher (e.g. *Pbca*) symmetry.

Both β-opx and α-popx have double the number of symmetrically unique sites as both the initial opx structure and γ-opx: 4 Mg, 4 Si, and 12 O (Table 3b). However, as with γ-opx, both of the A-chains (Aa and Ab) are S-rotated and both of the B-chains (Ba and Bb) are O-rotated. Unlike β- or γ-opx, though, α-popx has a portion of its Si sites coordinated by more than four O anions. The Si cations in the Ab chain can be described as 4+1 coordinated in a distorted square pyramid configuration (Figure 6). At 34 GPa, four of the Si-O bonds are similar in length, and range from 1.581-1.688 Å, while the fifth bond is a significantly longer 2.181 Å. The next shortest Si-O distance (not a bond), which would complete a distorted octahedron around the central Si, is 2.550 Å.

Although the fifth bond distance is significantly longer than the other four, our procrystal electron density analysis explicitly found a bond path between the relevant Si and the fifth oxygen. We adopt the notation 4+1 notation to denote that the length of this bond is significantly different from the four other Si-O bonds, and consider the Si cations in the Ab chain to be in highly distorted 5-coordination with O. The long bond in the SiO_5 polyhedron connects the Si cations in the Ab chain with adjacent Si cations in the Aa chain through a bridging O anion, resulting in the loss of the isolated Si-chain topology within the layer. In contrast, the Ba and Bb Si chains

296 remain nearly identical to their configuration in the initial opx structure, but with
297 increased O-rotation.
298 After additional compression to 40.3 GPa, a new phase, β-popx, (Figure 7,
299 Table 4), appears. The A-chains remain similar to α-popx, with the four initial
300 tetrahedral Ab Si-O bond lengths remaining essentially unchanged and ranging from
301 1.576-1.686 Å at 48.0 GPa. On the other hand, the long Si-O bond significantly
302 shortens, with a new length of 1.916 Å. However, the major rearrangement in this
303 structure occurs in the B-chains. While these chains previously contained only
304 tetrahedrally coordinated Si and were isolated from each other, in β-popx they form
305 a honeycombed sheet of edge-sharing, slightly distorted, Si-O octahedra (Figure 7).
306 This layer is nearly identical to the octahedral Si layer in the ilmenite-structured
307 high-P-T phase akimotoite (Horiuchi et al., 1982). In order for the Si cations to
308 become octahedrally coordinated, the Ba and Bb chains shift relative to each other
309 such that the Si octahedra line up in the *b*-direction. Significant diffuse scattering
310 observed in the *a**-direction of the diffraction patterns (Figure 3d) is likely due to
311 stacking faults between Mg and Si layers perpendicular to the *a*-direction of β-popx,
312 potentially due to the shifting Si B-chains.
313 Recently, Plonka et al. (2012) reported a new high-pressure monoclinic
314 phase of $CaMgSi_2O_6$ diopside, β-diopside. The relationship between the β-diopside
315 structure and the β-popx structure is analogous to that between cpx and opx. The
316 Mg octahedral layers are arranged perpendicular to the *a*-axis in a ++++ stacking in
317 cpx structures and a ++--++-- stacking in opx structures (+ and – represent tilting of
318 Mg octahedra in opposite directions (Papike et al., 1973)). These stacking patterns

remain in high-pressure β-diopside and β-popx. In addition, the B-chain octahedral Si layers in both structures are nearly identical. However, β-diopside retains only tetrahedral Si in its A-chains, whereas the Si in β-popx's Ab-chains is entirely 4+1-coordinated.

A Raman spectroscopy study by Serghiou et al. (2000) reported compression of single crystals of En_{100} opx to a maximum pressure of 70 GPa. Between ~7-15 GPa, new Raman peaks appeared that can be interpreted as corresponding to the $P2_1/c$ β-opx phase transition described by Zhang et al. (2012). The most drastic change in the Raman spectra occurred between ~38-40 GPa, where the Raman bands attributed to tetrahedrally-coordinated Si disappear and bands attributed to octahedrally-coordinated Si appear. The Raman spectra above 40 GPa also exhibit a poorer signal-to-noise ratio and broader peaks, which may be indicative of some crystallographic disorder and/or differential stress. On decompression, the higher pressure transition is reversible with a hysteresis of ~9 GPa, and the crystal eventually returns to the initial opx structure below 10 GPa (Serghiou et al., 2000).

Our experiments show transition pressures that are generally consistent with those reported in Serghiou et al. (2000), although there is no evidence in the Raman spectra for the β-opx to α-popx transition near 30 GPa. This transition may not have a strong spectroscopic signature. For the transition near 40 GPa, our results are consistent with the Raman study in that octahedral Si forms across the α-popx to β-popx transition and β-popx shows evidence for structural disorder. Upon further compression, Serghiou et al. (2000) find no additional changes in the Raman spectra to 70 GPa, which suggests that β-popx may remain present to this pressure.

342 It should be noted that Raman experiments used an argon pressure medium, which
343 is less hydrostatic than the neon medium used here. Therefore, there are likely some
344 differences in stress conditions between the two experiments.

345 Five-coordinated Si polyhedra, such as found here for α- and β-popx, are
346 unusual in that there are only a few previously reported cases of pentacoordinated
347 silicon in inorganic silicate crystals or glasses (although 5-coordinated organic Si
348 compounds are not uncommon (Liebau, 1984)). Pentacoordinated Si is observed in
349 minor quantities in silicate glasses at ambient pressure (Stebbins, 1991; Stebbins
350 and Poe, 1999). This five-coordinated fraction is reported to increase with pressure
351 as the glass structure evolves towards octahedral coordination at high pressure
352 (Stebbins and Poe, 1999; Williams and Jeanloz, 1988). Similar observations have
353 been reported in GeO_2 glasses that are analogs for SiO_2 (Guthrie et al., 2004). Only a
354 single experimentally determined silicate crystal structure with high concentrations
355 of SiO_5 units, a triclinic form of $CaSi_2O_5$, has been reported (Angel et al., 1996).
356 Subsequent studies investigated this phase's thermodynamic stability (Schoenitz et
357 al., 2001; Warren et al., 1999) and formation mechanism (Yu et al., 2013). Another
358 experimental study observed the formation of a small number of $(Si,Al)O_5$ units after
359 the dehydration and rehydration of the zeolite brewsterite (Alberti et al., 1999).
360 There are additional theoretical predictions for the formation of a 5-coordinated
361 SiO_2 structure in the presence of nonhydrostatic stress (Badro et al., 1997), and
362 more relevant to our experiments, molecular dynamics simulations by Chaplot and
363 Choudhury (2001) on En_{100} opx that suggest the formation of a structure with
364 disordered 5-coordinated Si at moderately high temperature. This structure is

predicted to exist at 15 GPa and 900 K, and is intermediate between opx and perovskite. We show here experimentally that the application of pressure at room temperature can yield structures with 5-coordinated Si, albeit highly distorted. Studies of additional pyroxenes or other silicates under room-temperature compression may yield phase transition sequences that also result in five-coordinated silicon.

Just as glasses can be thought of as overcooled liquids that are kinetically inhibited from crystallizing, opx is kinetically inhibited above ~25 GPa and 300 K from transforming to the thermodynamically stable six-coordinated perovskite structure. Therefore, it can only accommodate increasing compression through small translations of atoms (i.e. displacive mechanisms). As pressure increases and neighboring Si-O polyhedra are pushed closer together, new bonds bridging the polyhedra are formed, and the structure becomes increasingly polymerized. The bridging O anions appear to be able to be captured either one or two at a time (e.g. the A-chains vs. the B-chains), resulting in structures with mixed, 4-, 4+1-, and 6-coordinated Si-O polyhedra. It seems likely that this incremental polymerization mechanism would play a role in the 300 K high-pressure behavior of other chain silicates, or other types of silicates such as ring silicates. However, to date there have been limited quasi-hydrostatic single-crystal diffraction studies on cold-compressed silicates at pressures greater than ~15 GPa. While the high-pressure opx phase transitions appear to be reversible, five-coordinated structures could potentially be quenched in other compression environments such as those found in laboratory shock experiments or meteorite impacts.

388 We have chosen to differentiate between the two new structures described
389 here from the lower-pressure pyroxenes due to their >4-coordinated Si and the
390 similarity of β-popx to β-diopside. We therefore propose a new family of high-
391 pressure "post-pyroxene" structures that have pyroxene-like M1 and M2 sites
392 (holding Mg, Fe, Ca, etc. cations) interleaved with sheets of interlinked akimotoite-
393 like octahedral, or near-octahedral (i.e. >4 coordinated), Si cations. It is likely that a
394 number of these structures can be found at high pressure, with differences resulting
395 from the stacking and kinking arrangements of their respective precursor
396 pyroxenes. Raman spectroscopy shows that some pyroxenoids (e.g. $CaSiO_3$
397 wollastonite) also transform to dense crystalline high-pressure phases at 300 K on
398 compression (Serghiou, 2003), and future work should investigate the relationship
399 between these structures and post-pyroxenes.
400 Figure 8 summarizes the phase diagram of the $MgSiO_3$ system (after Fei and
401 Bertka (1999) and Presnall (1995)) together with estimated geotherms for normal
402 mantle (Brown and Shankland, 1981) and the coldest part of an old and fast
403 subducting slab (Bina and Navrotsky, 2000). Estimated P-T paths for shock-
404 compressed $MgSiO_3$ crystals and glass are also shown (Akins et al., 2004). $MgSiO_3$
405 phase boundaries are constrained by laboratory experiments only above ~1000 K
406 (Fei et al., 1990; Sawamoto, 1987). The coldest subducting slabs (e.g. Tonga) fall in a
407 temperature range below the mantle geotherm, as do the temperatures achieved in
408 dynamic compression experiments at upper mantle pressures. In the case of cold
409 subducting slabs, there is limited information on the kinetics of phase transitions at
410 the relevant temperatures. If transitions (e.g. the dissolution of cpx into garnet (van

Mierlo et al., 2013)) are kinetically inhibited on a geological time scale, metastable phases may persist in these environments. Furthermore, it should be recognized that there is also the possibility of phases undergoing structural distortions to metastable intermediates at moderate temperatures before fully transforming to the stable high-temperature phase. Such metastable phases might also be found in meteorites and impact sites, or lab-recovered shocked samples.

Conclusions

En_{90} opx was compressed to 48.5 GPa at 300 K while being probed with synchrotron-based single-crystal X-ray diffraction to monitor pressure-induced crystallographic changes. We observed the transformation of opx to the recently described β-opx phase at 14.6 GPa, as well as transformations to two metastable structures, α-popx and β-popx at 29.9 and 40.3 GPa, respectively. Both of the latter structures can be described with space group $Pca2_1$, which had previously been predicted as a possible pyroxene space group. The new phases have 4+1-coordinated Si, and, in the case of β-popx, also 6-coordinated Si. They are part of a recently discovered and growing pool of experimentally observed structures that show the ability of silicates with 4-coordinated Si to transform to denser 6-coordinated structures at ambient temperature. These transformations occur primarily by displacive mechanisms, allowing retention of the single crystal across the boundary, and may be relevant to the dynamics of cold subducting slabs. Additional work is needed on the kinetics of these metastable transformations at elevated temperatures to better understand their relationship with the

433 thermodynamically stable phases and their potential formation in geological
434 environments.

435 **Acknowledgements**

436 We thank the staffs of GSECARS and HPCAT for experimental assistance.
437 Robert Downs (Arizona) provided the procrystal bonding analysis software and
438 Nancy Ross (Virginia Tech) assisted with its use. We thank Jeremy Delaney
439 (Rutgers) for assistance with microprobe measurements. This work was supported
440 by the National Science Foundation. Portions of this work were performed at
441 GSECARS (Sector 13) and HPCAT (Sector 16), Advanced Photon Source, Argonne
442 National Laboratory. GSECARS and HPCAT are supported by the Department of
443 Energy and National Science Foundation. Use of the gas loading system was
444 supported by GSECARS and COMPRES.

445
446
447
448
449
450
451
452
453
454
455

References

Akins, J.A., Luo, S.-N., Asimow, P.D., Ahrens, T.J., 2004. Shock-induced melting of $MgSiO_3$ perovskite and implications for melts in Earth's lowermost mantle. Geophysical Research Letters 31.

Alberti, A., Sacerdoti, M., Quartieri, S., Vezzalini, G., 1999. Heating-induced phase transformation in zeolite brewsterite: New 4-and 5-coordinated (Si, Al) sites. Physics and Chemistry of Minerals 26, 181-186.

Angel, R.J., Bujak, M., Zhao, J., Gatta, G.D., Jacobsen, S.D., 2007. Effective hydrostatic limits of pressure media for high-pressure crystallographic studies. Journal of Applied Crystallography 40, 26-32.

Angel, R.J., Chopelas, A., Ross, N.L., 1992. Stability of high-density clinoenstatite at upper-mantle pressures. Nature 358, 322-324.

Angel, R.J., Hugh-Jones, D.A., 1994. Equations of state and thermodynamic properties of enstatite pyroxenes. Journal of Geophysical Research-Solid Earth 99, 19777-19783.

Angel, R.J., Jackson, J.M., 2002. Elasticity and equation of state of orthoenstatite, $MgSiO_3$. American Mineralogist 87, 558-561.

Angel, R.J., Ross, N.L., Seifert, F., Fliervoet, T.F., 1996. Structural characterization of pentacoordinate silicon in a calcium silicate. Nature 384, 441-444.

Bader, R.F.W., 1990. Atoms in molecules: A quantum theory. Oxford University Press, U.K.

Bader, R.F.W., 1998. A bond path: A universal indicator of bonded interactions. The Journal of Physical Chemistry A 102, 7314-7323.

Badro, J., Teter, D.M., Downs, R.T., Gillet, P., Hemley, R.J., Barrat, J.-L., 1997. Theoretical study of a five-coordinated silica polymorph. Physical Review B 56, 5797-5806.

Bina, C.R., Navrotsky, A., 2000. Possible presence of high-pressure ice in cold subducting slabs. Nature 408, 844-847.

Brandenburg, K., Putz, H., 2009. Endeavour - Structure solution from powder diffraction. Crystal Impact.

487 Brown, J.M., Shankland, T.J., 1981. Thermodynamic parameters in the earth as
488 determined from seismic profiles. Geophysical Journal International 66, 579-596.

489 Bruker, 2007. XPREP. Bruker AXS Inc., Madison, Wisconsin, USA.

490 Chaplot, S.L., Choudhury, N., 2001. Molecular dynamics simulations of seismic
491 discontinuities and phase transitions of $MgSiO_3$ from 4 to 6-coordinated silicate via
492 a novel 5-coordinated phase. American Mineralogist 86, 752-761.

493 Dera, P., Finkelstein, G.J., Duffy, T.S., Downs, R.T., Meng, Y., Prakapenka, V., Tkachev,
494 S., 2013a. Metastable high-pressure transformations of orthoferrosilite Fs_{82}. Physics
495 of the Earth and Planetary Interiors 221, 15-21.

496 Dera, P., Zhuravlev, K., Prakapenka, V., Rivers, M.L., Finkelstein, G.J., Grubor-
497 Urosevic, O., Tschauner, O., Clark, S.M., Downs, R.T., 2013b. High pressure single-
498 crystal micro X-ray diffraction analysis with GSE_ADA/RSV software. High Pressure
499 Research, 1-19.

500 Domeneghetti, M.C., Tazzoli, V., Ballaran, T.B., Molin, G.M., 1996. Orthopyroxene
501 from the Serra de Mage Meteorite: A structure-refinement procedure for a Pbca
502 phase coexisting with a C2/c exsolved phase. American Mineralogist 81, 842-846.

503 Dorfman, S.M., Meng, Y., Prakapenka, V.B., Duffy, T.S., 2013. Effects of Fe-enrichment
504 on the equation of state and stability of $(Mg,Fe)SiO_3$ perovskite. Earth and Planetary
505 Science Letters 361, 249-257.

506 Downs, R.T., Andalman, A., Hudacsko, M., 1996. The coordination numbers of Na and
507 K atoms in low albite and microcline as determined from a procrystal electron-
508 density distribution. American Mineralogist 81, 1344-1349.

509 Downs, R.T., Bartelmehs, K., Sinnaswamy, K., 2003. XtalDraw.

510 Downs, R.T., Gibbs, G.V., Jr, M.B.B., Rosso, K.M., 2002. A comparison of procrystal and
511 ab initio model representations of the electron-density distributions of minerals.
512 Physics and Chemistry of Minerals 29, 369-385.

513 Dziewonski, A.M., Anderson, D.L., 1981. Preliminary reference Earth model. Physics
514 of the Earth and Planetary Interiors 25, 297-356.

515 Fei, Y., Bertka, C.M., 1999. Phase transitions in the earth's mantle and mantle
516 mineralogy. Mantle Petrology: Field Observations and High Pressure
517 Experimentation, 189-207.

518 Fei, Y., Ricolleau, A., Frank, M., Mibe, K., Shen, G., Prakapenka, V., 2007. Toward an
519 internally consistent pressure scale. Proceedings of the National Academy of
520 Sciences 104, 9182-9186.

521 Fei, Y., Saxena, S.K., Navrotsky, A., 1990. Internally consistent thermodynamic data
522 and equilibrium phase relations for compounds in the system MgO-SiO_2 at high
523 pressure and high temperature. Journal of Geophysical Research: Solid Earth 95,
524 6915-6928.

525 Guthrie, M., Tulk, C.A., Benmore, C.J., Xu, J., Yarger, J.L., Klug, D.D., Tse, J.S., Mao, H.k.,
526 Hemley, R.J., 2004. Formation and structure of a dense octahedral glass. Physical
527 Review Letters 93.

528 Hammersley, A.P., Svensson, S.O., Hanfland, M., Fitch, A.N., Hausermann, D., 1996.
529 Two-dimensional detector software: From real detector to idealised image or two-
530 theta scan. High Pressure Research 14, 235-248.

531 Hogrefe, A., Rubie, D.C., Sharp, T.G., Seifert, F., 1994. Metastability of enstatite in
532 deep subducting lithosphere. Nature 372, 351-353.

533 Horiuchi, H., Hirano, M., Ito, E., Matsui, Y., 1982. $MgSiO_3$ (ilmenite-type): Single-
534 crystal X-ray-diffraction study. American Mineralogist 67, 788-793.

535 Jahn, S., 2008. High-pressure phase transitions in $MgSiO_3$ orthoenstatite studied by
536 atomistic computer simulation. American Mineralogist 93, 528-532.

537 Kanzaki, M., 1991. Ortho/clinoenstatite transition. Physics and Chemistry of
538 Minerals 17, 726-730.

539 Kissel, L., Pratt, R.H., 1990. Corrections to tabulated anomalous-scattering factors.
540 Acta Crystallographica Section A: Foundations of Crystallography 46, 170-175.

541 Kung, J., Li, B., Uchida, T., Wang, Y., Neuville, D., Liebermann, R.C., 2004. In situ
542 measurements of sound velocities and densities across the orthopyroxene --> high-
543 pressure clinopyroxene transition in $MgSiO_3$ at high pressure. Physics of the Earth
544 and Planetary Interiors 147, 27-44.

545 Li, B., Kung, J., Liu, W., Liebermann, R.C., 2013. Phase transitions and elasticity of
546 enstatite under pressure from experiments and first-principles studies. Physics of
547 the Earth and Planetary Interiors.

548 Liebau, F., 1984. Pentacoordinate silicon intermediate states during silicate
549 condensation and decondensation. Crystallographic support. Inorganica Chimica
550 Acta 89, 1-7.

551 Lin, C.C., 2003. Pressure-induced metastable phase transition in orthoenstatite
552 ($MgSiO_3$) at room temperature: A Raman spectroscopic study. Journal of Solid State
553 Chemistry 174, 403-411.

554 Nishi, M., Kato, T., Kubo, T., Kikegawa, T., 2008. Survival of pyropic garnet in
555 subducting plates. Physics of the Earth and Planetary Interiors 170, 274-280.

556 Pacalo, R.E.G., Gasparik, T., 1990. Reversals of the orthoenstatite-clinoenstatite
557 transition at high pressures and high temperatures. Journal of Geophysical
558 Research: Solid Earth 95, 15853-15858.

559 Papike, J.J., Prewitt, C.T., Sueno, S., Cameron, M., 1973. Pyroxenes: Comparisons of
560 real and ideal structural topologies. Zeitschrift für Kristallographie 138, 254-273.

561 Periotto, B., Balić-Žunić, T., Nestola, F., Katerinopoulou, A., Angel, R.J., 2012. Re-
562 investigation of the crystal structure of enstatite under high-pressure conditions.
563 American Mineralogist 97, 1741-1748.

564 Plonka, A.M., Dera, P., Irmen, P., Rivers, M.L., Ehm, L., Parise, J.B., 2012. β-diopside, a
565 new ultrahigh-pressure polymorph of $CaMgSi_2O_6$ with six-coordinated silicon.
566 Geophysical Research Letters 39.

567 Presnall, D.C., 1995. Phase diagrams of Earth-forming minerals. Mineral Physics and
568 Crystallography: A Handbook of Physical Constants 2, 248-268.

569 Putz, H., Schön, J.C., Jansen, M., 1999. Combined method for ab initio structure
570 solution from powder diffraction data. Journal of Applied Crystallography 32, 864-
571 870.

572 Ringwood, A.E., 1975. Composition and petrology of the earth's mantle. McGraw-
573 Hill, New York.

574 Ringwood, A.E., 1982. Phase transformations and differentiation in subducted
575 lithosphere: Implications for mantle dynamics, basalt petrogenesis, and crustal
576 evolution. The Journal of Geology 90, 611-643.

577 Sawamoto, H., 1987. Phase diagram of $MgSiO_3$ at pressures up to 24 GPa and
578 temperatures up to 2200 °C: Phase stability and properties of tetragonal garnet, in:

579 Manghnani, M.H., Syono, Y. (Eds.), Geophysical Monograph Series. American
580 Geophysical Union, Washington, D. C., pp. 209-219.

581 Schoenitz, M., Navrotsky, A., Ross, N., 2001. Enthalpy of formation of $CaSi_2O_5$, a
582 quenched high-pressure phase with pentacoordinate silicon. Physics and Chemistry
583 of Minerals 28, 57-60.

584 Serghiou, G., 2003. High-pressure phase transitions in tetrahedrally coordinated
585 chain structures. Journal of Raman Spectroscopy 34, 587-590.

586 Serghiou, G., Boehler, R., Chopelas, A., 2000. Reversible coordination changes in
587 crystalline silicates at high pressure and ambient temperature. Journal of Physics:
588 Condensed Matter 12, 849-857.

589 Sheldrick, G.M., 2008. A short history of SHELX. Acta Crystallographica Section A:
590 Foundations of Crystallography 64, 112-122.

591 Smyth, J.R., 1974. Low orthopyroxene from a lunar deep crustal rock: A new
592 pyroxene polymorph of space group $P2_1ca$. Geophysical Research Letters 1, 27-29.

593 Stebbins, J.F., 1991. NMR evidence for five-coordinated silicon in a silicate glass at
594 atmospheric pressure. Nature 351, 638-639.

595 Stebbins, J.F., Poe, B.T., 1999. Pentacoordinate silicon in high-pressure crystalline
596 and glassy phases of calcium disilicate ($CaSi_2O_5$). Geophysical Research Letters 26,
597 2521-2523.

598 Sueno, S., Cameron, M., Prewitt, C.T., 1976. Orthoferrosilite: High-temperature
599 crystal chemistry. American Mineralogist 61, 38-53.

600 Takemura, K., Dewaele, A., 2008. Isothermal equation of state for gold with a He-
601 pressure medium. Physical Review B 78, 104119.

602 Tarantino, S.C., Domeneghetti, M.C., Carpenter, M.A., Shaw, C.J.S., Tazzoli, V., 2002.
603 Mixing properties of the enstatite-ferrosilite solid solution: I. A macroscopic
604 perspective. European Journal of Mineralogy 14, 525-536.

605 Thompson, J.B., 1970. Geometrical possibilities for amphibole structures: Model
606 biopyriboles. American Mineralogist 55, 292-293.

van Mierlo, W.L., Langenhorst, F., Frost, D.J., Rubie, D.C., 2013. Stagnation of subducting slabs in the transition zone due to slow diffusion in majoritic garnet. Nature Geoscience 6, 400-403.

Warren, M.C., Redfern, S.A.T., Angel, R., 1999. Change from sixfold to fivefold coordination of silicate polyhedra: Insights from first-principles calculations of $CaSi_2O_5$. Physical Review B 59.

Williams, Q., Jeanloz, R., 1988. Spectroscopic evidence for pressure-induced coordination changes in silicate glasses and melts. Science 239, 902-905.

Woodland, A.B., 1998. The orthorhombic to high-P monoclinic phase transition in Mg-Fe pyroxenes: Can it produce a seismic discontinuity? Geophysical Research Letters 25, 1241-1244.

Yang, H., Finger, L.W., Conrad, P.G., Prewitt, C.T., Hazen, R.M., 1999. A new pyroxene structure at high pressure: Single-crystal X-ray and Raman study of the Pbcn-$P2_1cn$ phase transition in protopyroxene. American Mineralogist 84, 245-256.

Yu, Y.G., Angel, R.J., Ross, N.L., Gibbs, G.V., 2013. Pressure impact on the structure, elasticity, and electron density distribution of $CaSi_2O_5$. Physical Review B 87.

Zhang, D., Jackson, J.M., Chen, B., Sturhahn, W., Zhao, J., Yan, J., Caracas, R., 2013a. Elasticity and lattice dynamics of enstatite at high pressure. Journal of Geophysical Research: Solid Earth 118, 4071-4082.

Zhang, D., Jackson, J.M., Sturhahn, W., Xiao, Y., 2011. Local structure variations observed in orthoenstatite at high pressures. American Mineralogist 96, 1585-1592.

Zhang, J.S., Dera, P., Bass, J.D., 2012. A new high-pressure phase transition in natural Fe-bearing orthoenstatite. American Mineralogist 97, 1070-1074.

Zhang, J.S., Reynard, B., Montagnac, G., Bass, J.D., 2014. Pressure-induced Pbca–$P2_1/c$ phase transition of natural orthoenstatite: The effect of high temperature and its geophysical implications. Physics of the Earth and Planetary Interiors 228, 150-159.

Zhang, J.S., Reynard, B., Montagnac, G., Wang, R.C., Bass, J.D., 2013b. Pressure-induced Pbca-$P2_1/c$ phase transition of natural orthoenstatite: Compositional effect and its geophysical implications. American Mineralogist 98, 986-992.

Tables

Table 1. Orthopyroxene composition

Oxide	Weight %
MgO	35.17
FeO	6.13
Al_2O_3	0.21
SiO_2	58.19
CaO	0.18
MnO	0.22
Total	100.1

The chemical formula is $Mg_{0.900}Fe_{0.088}Ca_{0.003}Mn_{0.003}Al_{0.004}Si_{0.999}O_3$.

Table 2. Lattice parameters and volumes of opx phases

Orthopyroxene

Au *a* (Å)	P (GPa)	*a* (Å)	*b* (Å)	*c* (Å)	V (Å^3)
	0	18.249(2)	8.8263(9)	5.1858(3)	835.30(14)
4.0645	1.8	18.173(3)	8.7805(12)	5.1622(2)	823.70(15)
4.0469	4.2	18.099(3)	8.7136(15)	5.1317(3)	809.30(19)
4.0298	6.7	18.019(3)	8.6417(12)	5.1040(2)	794.76(16)
4.0085	10.1	17.915(3)	8.5730(13)	5.0715(3)	778.89(17)

β-Orthopyroxene

Au *a* (Å)	P (GPa)	*a* (Å)	*b* (Å)	*c* (Å)	*β* (°)	V (Å^3)
3.9832	14.6	17.903(6)	8.520(3)	4.9325(5)	92.826(12)	751.5(4)
3.9633	18.5	17.799(5)	8.472(3)	4.8987(4)	93.029(10)	737.6(3)
3.9417	23.0	17.702(5)	8.398(3)	4.8629(5)	93.141(11)	721.9(3)
3.9248	26.9	17.583(6)	8.350(3)	4.8348(6)	93.388(16)	708.6(4)

α-Post-Orthopyroxene

Au *a* (Å)	P (GPa)	*a* (Å)	*b* (Å)	*c* (Å)	V (Å^3)
3.9121	29.9	17.595(4)	8.3658(15)	4.6957(3)	691.20(18)
3.8962	34.0	17.492(4)	8.2782(19)	4.6580(3)	674.5(3)
3.8861	36.8	17.435(4)	8.215(3)	4.6455(4)	665.4(3)

β-Post-Orthopyroxene

Au *a* (Å)	P (GPa)	*a* (Å)	*b* (Å)	*c* (Å)	V (Å^3)
3.8738	40.3	17.445(8)	8.011(4)	4.5747(7)	639.3(4)
3.8601	44.4	17.416(5)	7.925(3)	4.5447(5)	627.3(3)
3.8470	48.5	17.377(6)	7.847(3)	4.5268(5)	617.3(3)

Table 3

a) Representative single-crystal structure refinement for α-post-orthopyroxene.

Beamline	13 ID-D, GSECARS, APS, ANL
Wavelength (Å)	0.295
Pressure (GPa)	34.0
Temperature (K)	298
Composition	$Mg_{0.90}Fe_{0.1}SiO_3$
Symmetry	Orthorhombic, $Pca2_1$
Lattice Parameters *a*, *b*, *c* (Å)	4.6580(3), 8.2782(19), 17.492(4)
Volume (Å^3)	674.5(2)
Z	8
R_{int}	0.072
Reflection Range	-8 ≤ h ≤ 8, -9 ≤ k ≤ 10, -22 ≤ l ≤ 23
Maximum θ (°)	33.94
Number Independent Reflections	553
Number Refined Parameters	85
Refinement	F^2
R1	0.046
wR_2	0.100
GooF	1.055

b) Refined atomic parameters. All atoms are in Wyckoff position 4a.

Atom	Site Occupancy	x/*a*	y/*b*	z/*c*	U_{iso}
Mg1a	0.963(16)	0.7869(9)	0.9088(9)	0.8121(5)	0.0061(9)
Mg1b	0.963(16)	0.8711(10)	0.4117(8)	0.5625(4)	0.0064(11)
Mg2a, Fe2a	0.879(16), 0.121(16)	0.7932(9)	0.2831(7)	0.8081(4)	0.0062(10)
Mg2b, Fe2b	0.879(16), 0.121(16)	0.8841(9)	0.7781(7)	0.5588(4)	0.0073(12)
SiAa	0.912(19)	0.4160(8)	0.9043(8)	0.6636(3)	0.0033(9)
SiAb	0.912(19)	0.8291(8)	0.5991(7)	0.7044(3)	0.0053(10)
SiBa	0.946(18)	0.1441(8)	0.9061(8)	0.9616(3)	0.0045(10)
SiBb	0.946(18)	0.7664(7)	0.5948(9)	0.9109(3)	0.0058(10)
O1	1	0.4399(15)	0.9122(18)	0.7510(7)	0.007(2)
O2	1	0.953(2)	0.7521(18)	0.7473(8)	0.009(3)
O3	1	0.1348(17)	0.9048(19)	0.8706(8)	0.009(3)
O4	1	0.5929(19)	0.4342(16)	0.8815(9)	0.008(3)
O5	1	0.6183(19)	0.7457(16)	0.8766(9)	0.008(3)
O6	1	0.0065(18)	0.4401(16)	0.7420(8)	0.010(3)
O7	1	0.7793(18)	0.5887(18)	0.0005(7)	0.007(2)
O8	1	0.8177(19)	0.9360(16)	0.9938(8)	0.009(3)
O9	1	0.0188(17)	0.5897(17)	0.6243(8)	0.0077(19)
O10	1	0.0972(18)	0.9409(16)	0.6291(9)	0.010(3)
O11	1	0.5652(19)	0.7480(16)	0.6293(8)	0.008(3)
O12	1	0.2743(19)	0.7547(15)	0.0013(8)	0.007(3)

Table 4

a) Representative single-crystal structure refinement for β-post-orthopyroxene.

Beamline	13 ID-D, GSECARS, APS, ANL
Wavelength (Å)	0.295
Pressure (GPa)	48.5
Temperature (K)	298
Composition	$Mg_{0.90}Fe_{0.1}SiO_3$
Symmetry	Orthorhombic, $Pca2_1$
Lattice Parameters *a*, *b*, *c* (Å)	4.5268(5), 7.847(3), 17.377(6)
Volume (Å^3)	617.3(3)
Z	8
R_{int}	0.066
Reflection Range	-7 ≤ h ≤ 7, -9 ≤ k ≤ 9, -18 ≤ l ≤ 22
Maximum θ (°)	30.01
Number Independent Reflections	440
Number Refined Parameters	85
Refinement	F^2
R1	0.059
wR_2	0.143
GooF	1.067

b) Refined atomic parameters. All atoms are in Wyckoff position 4a.

Atom	Site Occupancy	x/*a*	y/*b*	z/*c*	U_{iso}
Mg1a	0.99(4)	0.0466(18)	0.4101(17)	0.4313(5)	0.0059(19)
Mg1b	0.99(4)	0.4355(16)	0.0919(18)	0.1946(5)	0.0042(19)
Mg2a, Fe2a	0.83(4), 0.17(4)	0.5472(16)	0.2084(13)	0.4432(5)	0.0082(18)
Mg2b, Fe2b	0.83(4), 0.17(4)	0.4224(15)	0.7243(12)	0.1750(6)	0.0055(17)
SiAa	0.93(4)	0.4049(14)	0.4048(11)	0.2877(4)	0.0011(16)
SiAb	0.93(4)	0.0142(13)	0.1011(12)	0.3271(5)	0.0031(16)
SiBa	1.00(4)	0.4424(14)	0.4178(11)	0.0710(4)	0.0053(17)
SiBb	1.00(4)	0.4255(14)	0.0862(15)	0.0554(4)	0.0064(19)
O1	1	0.135(3)	0.443(3)	0.1214(11)	0.004(4)
O2	1	0.733(4)	0.062(4)	0.0063(11)	0.015(5)
O3	1	0.223(4)	0.243(4)	0.2557(11)	0.009(4)
O4	1	0.343(4)	0.065(3)	0.3646(11)	0.009(5)
O5	1	0.399(4)	0.406(3)	0.3779(11)	0.007(4)
O6	1	0.293(4)	0.265(3)	0.0085(10)	0.006(4)
O7	1	0.104(4)	0.071(3)	0.1193(10)	0.004(4)
O8	1	0.263(3)	0.578(3)	0.0094(9)	0.003(4)
O9	1	0.067(4)	0.758(3)	0.1181(9)	0.007(4)
O10	1	0.734(4)	0.432(3)	0.2553(9)	0.003(4)
O11	1	0.867(4)	0.249(3)	0.3750(12)	0.011(4)
O12	1	0.779(4)	0.091(3)	0.2520(10)	0.006(4)

672 **Figure Captions**

673

674 Figure 1. The orthopyroxene structure. Si tetrahedra are blue and Mg octahedra are
675 gray. Polyhedra labeled 1 and 2 are symmetrically distinct Mg sites, and those
676 labeled A and B are symmetrically distinct Si sites. Mg/Si a, b, c, and d are layers in
677 the orthopyroxene *bc* plane that are shown in detail on the right half the figure.

678

679 Figure 2. Sample configuration showing five orthopyroxene crystals, a ruby ball, and
680 a gold foil immersed in a liquid neon pressure-transmitting medium and contained
681 in a diamond-anvil cell. The data reported in this paper are from the crystal denoted
682 by the arrow.

683

684 Figure 3. Left: Example diffraction pattern for α-popx at 34.0 GPa using the center
685 detector position. The black box indicates the zoomed-in region used to illustrate
686 different phases on the right. Right: a) *Pbca* opx at 1.8 GPa. The small spots are
687 diffraction peaks from the opx crystal. Also visible are diamond peaks (large spots)
688 and powder rings from Au and neon. b) $P2_1/c$ β-opx diffraction at 18.5 GPa. The
689 inset shows peak doubling due to non-merohedral twinning. c) $P2_1ca$ α-popx
690 diffraction at 34.0 GPa. Crystal is untwinned. d) $P2_1ca$ β-popx diffraction at 48.5 GPa.
691 The inset shows diffuse scattering between peaks in the a^*-direction of reciprocal
692 space. This is likely due to stacking faults along (100).

693

694 Figure 4. Unit-cell volume of En_{90} orthopyroxene and its high-pressure polymorphs
695 from this study (black symbols) compared to previous single-crystal En_{100}
696 orthopyroxene (red symbols) (Angel and Hugh-Jones, 1994; Angel and Jackson,
697 2002) and En_{16} orthopyroxene experiments (open symbols) (Dera et al., 2013a).
698 Error bars are smaller than the symbol size. Fits to the data are shown as a visual
699 guide. The colored regions denote the observed pressure ranges for orthopyroxene
700 polymorphs at 300 K in both the En_{90} (top) and En_{16} (bottom) compositions.
701
702 Figure 5. Axial compression of En_{90} orthopyroxene and its high pressure
703 polymorphs (relative to the ambient orthopyroxene lattice parameters) from this
704 study (black symbols) compared to previous single-crystal En_{16} orthopyroxene
705 experiments (open symbols). Error bars are smaller than the symbol size. Fits to the
706 data are shown as a visual guide. The colored regions denote the observed pressure
707 ranges for 300 K, high-pressure orthopyroxene polymorphs at 300 K in both the
708 En_{90} (top) and En_{16} (bottom) compositions.
709
710 Figure 6.The α-popx structure at 34.0 GPa. Si polyhedra are blue and Mg polyhedra
711 are gray. Polyhedra labeled 1a,b and 2a,b are symmetrically distinct Mg sites, and
712 those labeled Aa,b and Ba,b are symmetrically distinct Si sites. Mg/Si a, b, c, and d
713 are layers in the α-popx *bc* plane that are shown in detail on the right half the figure.
714
715 Figure 7. The β-popx structure at 48.5 GPa. Si polyhedra are blue and Mg polyhedra
716 are gray. Polyhedra labeled 1a,b and 2a,b are symmetrically distinct Mg sites, and

those labeled Aa,b and Ba,b are symmetrically distinct Si sites. Mg/Si a, b, c, and d are layers in the β-popx *bc* plane that are shown in detail on the right half the figure.

Figure 8. Synthesis of high-pressure data for $MgSiO_3$ polymorphs, including observed 300 K En_{90} orthopyroxene phases in this study. Sources are: $MgSiO_3$ phase diagram (after Fei and Bertka (1999) and Presnall (1995)), normal mantle (Brown and Shankland, 1981) (depth-pressure conversion from (Dziewonski and Anderson, 1981))and cold slab (Bina and Navrotsky, 2000) geotherms, and $MgSiO_3$ glass and enstatite shock compression Hugoniots (Akins et al., 2004). The abbreviations stand for: oen – orthoenstatite, pen – protoenstatite, lpcen – low-pressure $P2_1/c$ clinoenstatite, hpcen – high-pressure $C2/c$ clinoenstatite, maj – majorite garnet, wad – wadsleyite, st – stishovite, rwd – ringwoodite, akm – akimotoite, pv – perovskite, and Hug. – Hugoniot.

Figure 1

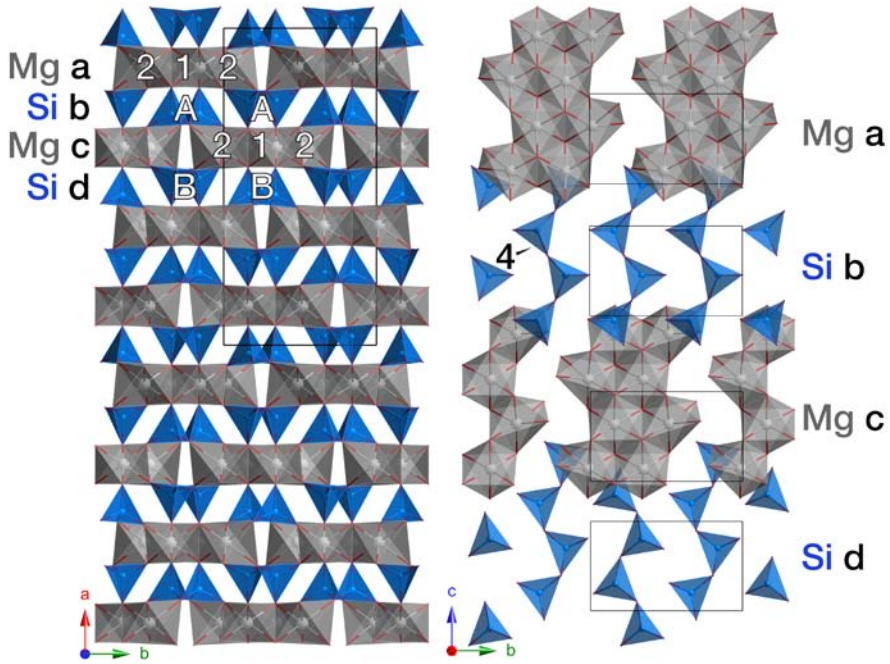

Figure 2

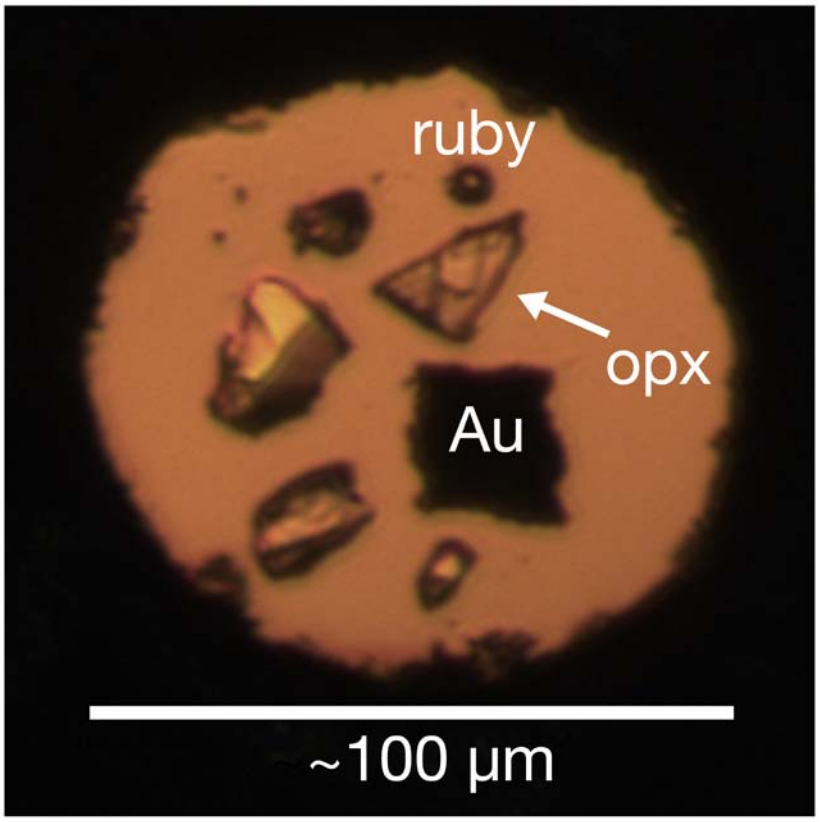

752
753

Figure 3

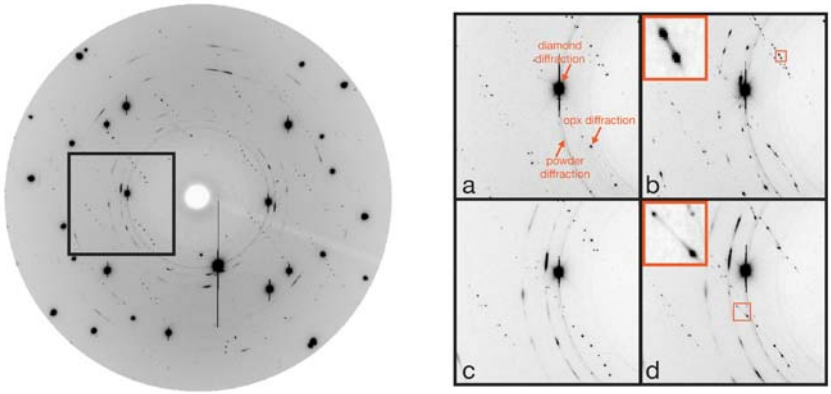

754
755

Figure 4

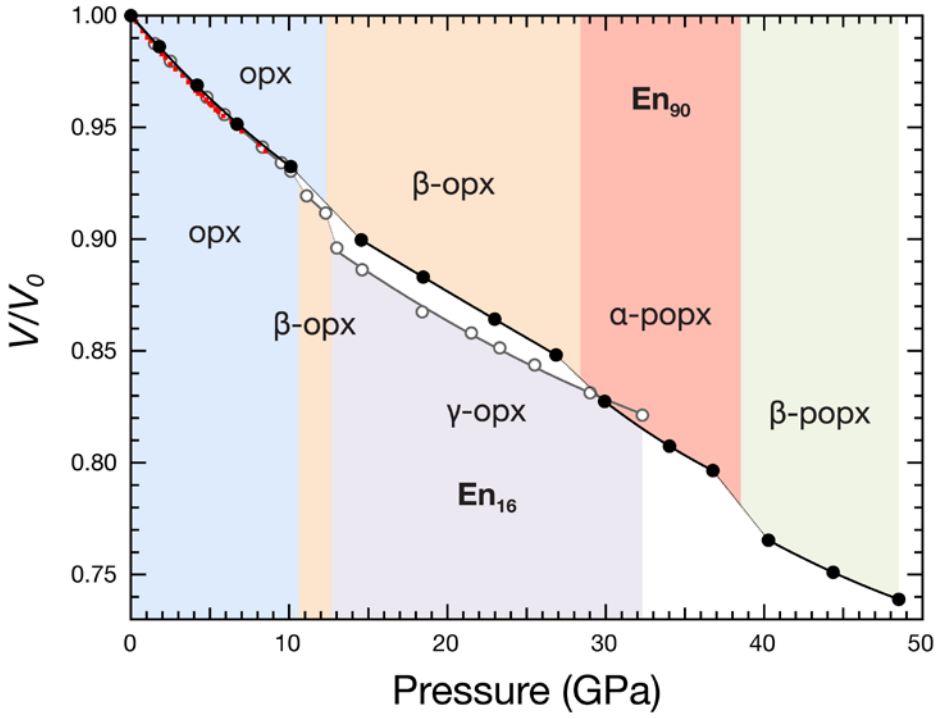
1.00
0.95
0.90
0.85
0.80
0.75
V/V0
0
10
20
30
40
50
Pressure (GPa)
opx
opx
β-opx
β-opx
γ-opx
En16
En90
α-popx
β-popx

Figure 5

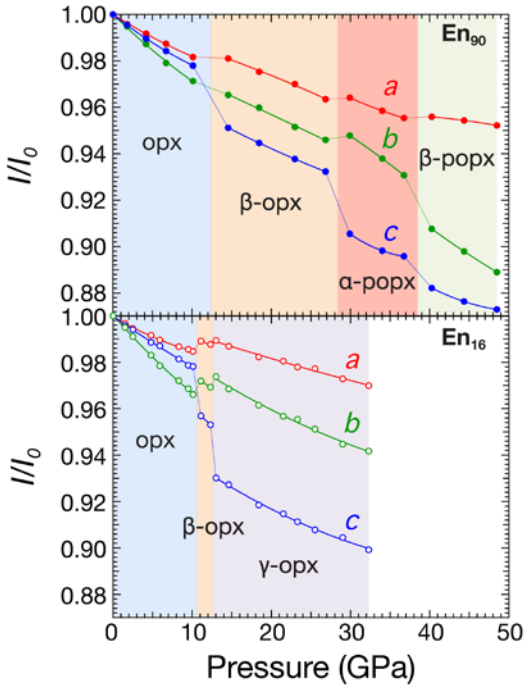

Figure 6

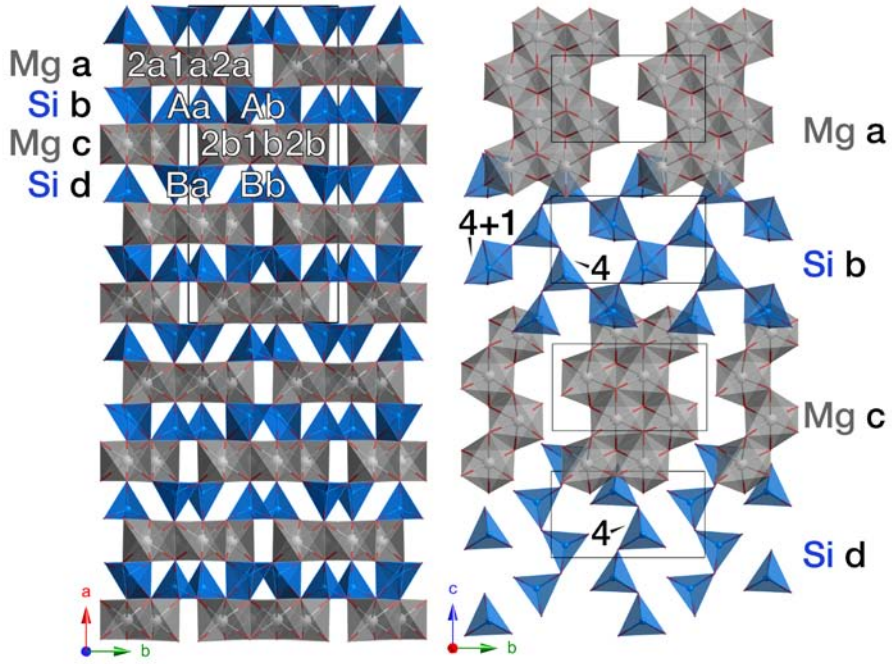

760
761

Figure 7

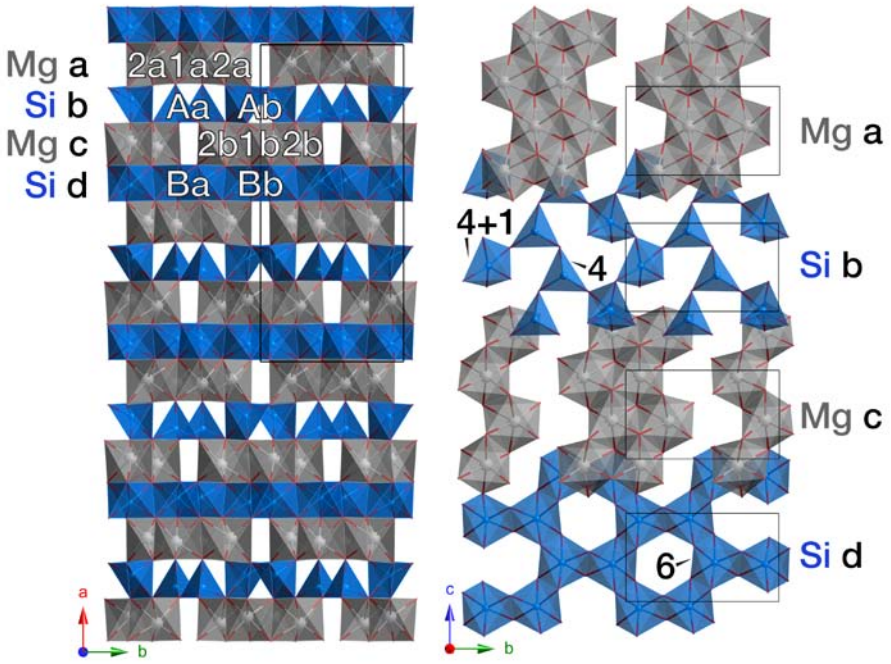

762
763

Figure 8

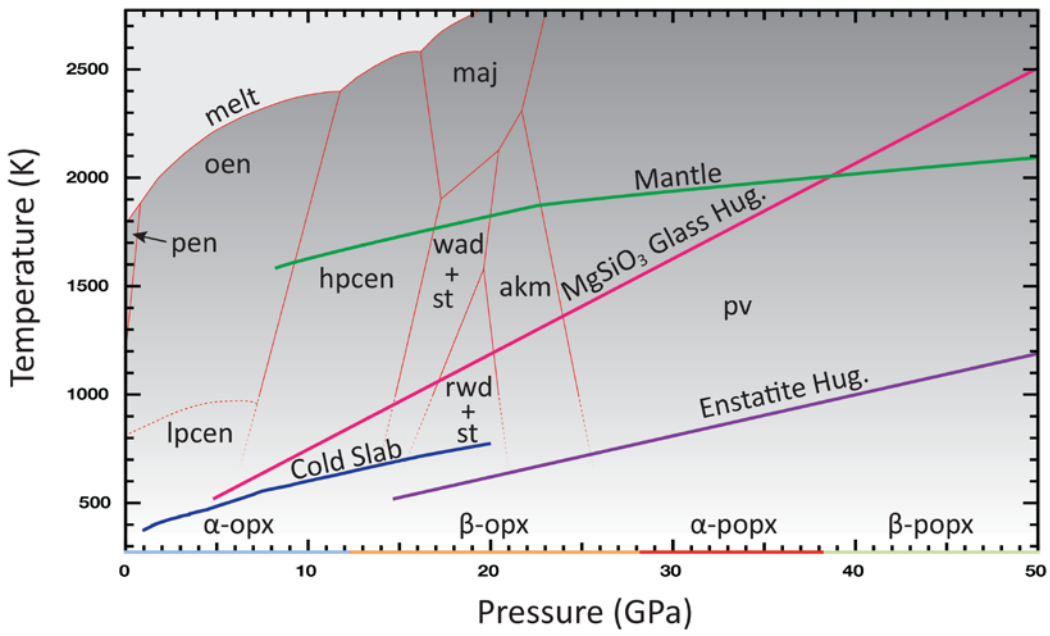
Temperature (K)
2500
2000
1500
1000
500
0
10
20
30
40
50
Pressure (GPa)
melt
oen
pen
maj
Mantle
hpcen
wad
+
st
akm
MgSiO3 Glass Hug.
pv
lpcen
rwd
+
st
Cold Slab
Enstatite Hug.
α-opx
β-opx
α-popx
β-popx

764